Laser-Induced Cavitation for Controlling Crystallization from Solution

Nagalingam, Nagaraj; Raghunathan, Aswin; Korede, Vikram; Poelma, Christian; Smith, Carlas S.; Hartkamp, Remco; Padding, Johan T.; Eral, Hüseyin Burak

DOI
10.1103/PhysRevLett.131.124001

Publication date
2023

Document Version
Final published version

Published in
Physical review letters

Editors' Suggestion

Laser-Induced Cavitation for Controlling Crystallization from Solution

Nagaraj Nagalingam,[1] Aswin Raghunathan,[1] Vikram Korede,[1] Christian Poelma,[1] Carlas S. Smith,[2] Remco Hartkamp,[1] Johan T. Padding,[1] and Hüseyin Burak Eral[1,*]

[1]*Process and Energy Department, Delft University of Technology, Leeghwaterstraat 39, 2628 CB Delft, Netherlands*

[2]*Delft Center for Systems and Control, Delft University of Technology, Mekelweg 2, 2628 CD Delft, Netherlands*

(Received 3 February 2023; revised 17 July 2023; accepted 22 August 2023; published 18 September 2023)

We demonstrate that a cavitation bubble initiated by a Nd:YAG laser pulse below breakdown threshold induces crystallization from supersaturated aqueous solutions with supersaturation and laser-energy-dependent nucleation kinetics. Combining high-speed video microscopy and simulations, we argue that a competition between the dissipation of absorbed laser energy as latent and sensible heat dictates the solvent evaporation rate and creates a momentary supersaturation peak at the vapor-liquid interface. The number and morphology of crystals correlate to the characteristics of the simulated supersaturation peak.

DOI: 10.1103/PhysRevLett.131.124001

Controlling crystallization from solution, which is central to technological applications ranging from nanomaterial synthesis to pharmaceutical manufacturing [1–3], is still challenging our understanding of nucleation [4–6]. Among the strategies proposed to control kinetics and emerging crystal properties [7–9], nonphotochemical laser-induced nucleation (NPLIN), where one or more unfocused laser pulses trigger accelerated nucleation in supersaturated solutions [10–12], emerged as a promising approach due to its presumed nonchemical nature and ability to influence polymorphic form [13,14]. At the reported laser pulse duration (∼nanoseconds), wavelengths (532/1064 nm), and laser intensity (∼MW/cm^2), neither the solute nor the solvent have sufficiently strong absorption bands to induce photochemical effects. Several putative mechanistic hypotheses, ranging from molecular phenomena relying on (an)isotropic polarization and isotropic electronic polarizability of solute clusters [15] to microscale phenomena based on impurity heating and consequent cavitation, have been proposed in an attempt to explain the observations [16]. However, the exact mechanism behind NPLIN remains elusive [16].

Transient microvapor bubbles can be created in liquid environments with the absorption of laser pulses by dyes [17] and nanoparticles [18,19]. The impurity heating hypothesis suggests that laser energy absorbed by inherent insoluble impurities (such as nanoparticles) locally evaporates its surrounding solvent—consequently triggering solute nucleation. However, no direct measurements of this hypothesized phenomenon were reported. Most reported NPLIN experiments only quantify the crystallization probability seconds to minutes after laser irradiation [20]. Moreover, the large exposed volumes [O(cm^3)] and uncertainties in concentration and chemical nature of impurities limit the observation of micron-sized cavitation bubbles within microseconds after laser irradiation. Thus, the attempts to test the impurity heating hypothesis using numerical modeling have had limited success due to lack of concomitant experimental data [21].

In this Letter, using high-speed microscopy experiments and 1D finite element simulations, we demonstrate that a momentary supersaturation rise surrounding a laser-induced cavitation bubble can trigger crystallization in supersaturated aqueous solutions of potassium chloride (KCl). We use a frequency-doubled Nd:YAG pulsed laser with 532 nm wavelength and 4 ns pulse duration. Unlike the traditional NPLIN experiments, we focus the laser to fix the location of bubble formation and intentionally dope the solution with a light-absorbing soluble impurity. We add 3.26 mg potassium permanganate ($KMnO_4$) per 100 g water to facilitate bubble formation below the optical breakdown threshold via thermocavitation [22] (see Supplemental Material [23], Sec. I). The laser focal spot resembles an impurity being heated up and a consequent cavitation bubble formation, establishing the connection between NPLIN experiments conducted with unfocused laser and this study. The added $KMnO_4$ is comparable to the impurities level in traditional NPLIN experiments [O(10 ppm)] [51] and therefore does not alter the solubility of KCl (see Supplemental Material [23], Sec. II). Thus, this work differentiates itself from cavitation-induced crystallization experiments via multiphoton absorption using focused ultrashort laser pulse (∼femtosecond) that might involve photochemistry [52]. Moreover, it captures the size of cavitation bubbles [O(100 μm)] [19] surrounding the nanoparticles for the inferred magnitude of laser energies and impurity sizes in NPLIN experiments [51] (see Supplemental Material [23], Sec. III for calculations).

We perform experiments to record the size of the vapor bubbles created, the resulting number and morphology of crystal(s) formed, and the cumulative nucleation probability at a fixed time lag. Subsequently, using simulations,

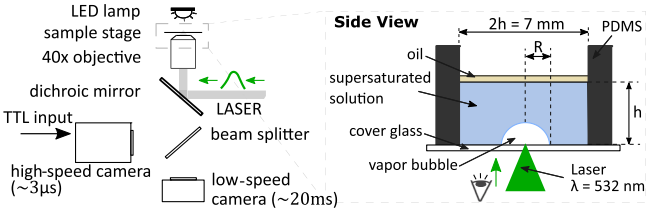

FIG. 1. Sketch of the experimental setup to generate a microbubble. The setup construction is detailed in our previous work [55]. The green arrow indicates the direction of laser pulse. PDMS: polydimethylsiloxane. TTL: transistor-transistor logic signal.

we estimate the local temperature, solute concentration, and solute supersaturation surrounding the bubble to complement the experiments. The quantitative agreement between experimental and simulated bubble dynamics validates the proposed model. Leveraging the model, we argue that a competition between the dissipation of absorbed laser energy as latent and sensible heat dictates the instantaneous solvent evaporation rate. A spike in evaporation rate during the cavitation bubble expansion creates a momentary supersaturation peak at the vapor-liquid interface (hereinafter referred to as "interface"). The experimentally acquired nucleation probabilities, number, and morphology of crystals formed correlate with the characteristics of the short-lived $[O(\mu s)]$ supersaturation peak surrounding the bubble from simulations. For the first time, we quantitatively correlate the likelihood of crystal formation due to an increase in the solute concentration at the interface through laser-induced bubble formation with no expected photochemical reaction.

In our experiments, KCl solutions with a supersaturation range of 0.999–1.029 were used (solubility = 35.97 g/100 g-H_2O at 25 °C) with no pretreatment for dissolved gases or filtration. A 40× objective (numerical aperture = 0.6) is employed to both focus the laser and image the sample. Figure 1 shows the architecture of the inverted microscope that employs two cameras: a high-speed camera operated at 330 000 frames/s to record the evolution of the bubble size and a low-speed camera operated at 50 frames/s, which records the appearance of crystals. A 1.23 mm layer of silicone oil (density = 930 kg/m^3) floating on top of the supersaturated solution prevents evaporation of the solution. The laser is focused to a point within 10 μm above the bottom surface (cover glass). The standoff distance to the bottom surface is maintained below 0.05 to prevent surface erosion [53]. In addition, all formed hemispherical bubbles in this work have $h/R_{max} > 10$ to prevent the effect of sidewalls on the bubble dynamics [54]. Thus, the cover glass acts as a plane of symmetry for the semiunbounded fluid surrounding the hemispherical bubble, allowing us to analyze the bubble as spherically unbound—a 3D bubble. Since the negatively buoyant crystals sediment to the bottom, the adapted experimental technique allows *in situ* recording of both the bubble and crystal(s).

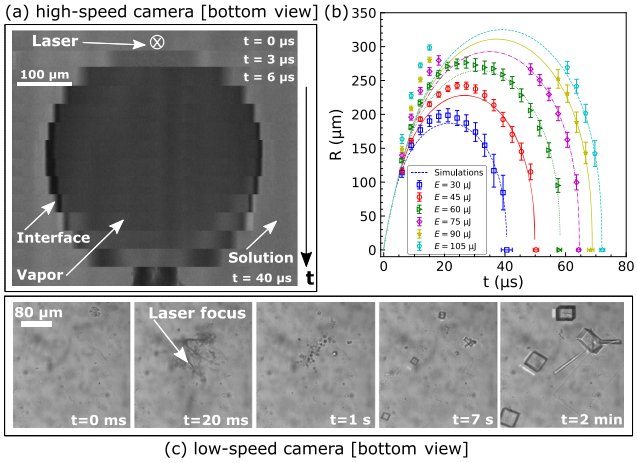

FIG. 2. (a) Primary vapor bubble formation using a focused laser pulse of 30 μJ recorded at 330 000 frames/s with a reduced spatial resolution. (b) Dynamic radius of the hemispherical bubble for different laser energies E. The error bars represent the standard error on the mean of at least 20 independent trials. A bubble radius beyond ≈300 μm exceeded the field of view of the camera. The symbols and lines correspond to experiments and simulations, respectively. (c) Secondary bubbles and emergence of crystals after collapse of the primary vapor bubble surrounding the laser focal spot visualized at 50 frames/s using the low-speed camera. The experiment is for $E = 75$ μJ and $S = 1.019$.

Figure 2(a) depicts the primary bubble formation, its subsequent expansion, and collapse immediately after laser irradiation. The primary bubble then disintegrates into secondary bubbles followed by the emergence of crystals surrounding the laser focal point [Fig. 2(c)]. After the primary bubble collapsed, we also observe a complex flow pattern that transports secondary bubbles and crystals. The direction of the resulting flow was observed to be random, consistent with previous observations [56]. Figure 2(b) displays a clear increase in the maximum radius (R_{max}) and bubble lifetime with the supplied laser energy (E). For details on the experimental methodology and validity of the bubble shape, see Supplemental Material [23], Sec. IV.

We quantify crystallization by plotting nucleation probability and crystal count for varying laser energy and supersaturation in the bulk, Fig. 3. The cumulative nucleation probability (p) is defined as the number of trials that resulted in crystal formation 2 min after laser irradiation to the number of trials performed. Overall, the nucleation probability increases with increasing laser energy and solution supersaturation in the bulk (S_{bulk}). From Fig. 3(a), we observe a minimum threshold laser energy for crystal formation related to S_{bulk} and vice versa, an observation repeatedly reported in NPLIN experiments [20]. We recorded a very low crystallization probability ($p \leq 0.1$) for roughly saturated solution ($S_{bulk} = 0.999$) as the lack of supersaturation would inhibit crystal growth.

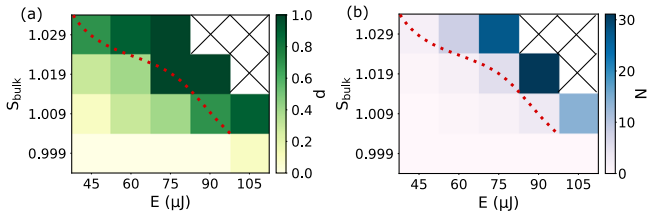

FIG. 3. Experimentally observed nucleation statistics: (a) cumulative nucleation probability (p) and (b) mean crystal count (N), for different laser energies (E) and solution supersaturation in the bulk (S_{bulk}). The results are for ten trials, each with a fixed lag of 2 min from the time of laser irradiation. The red dotted curve is a guide to the eye representing the threshold where the crystallization probability is ≥ 0.5. See Supplemental Material [23], Sec. V for morphologies.

We attribute the nonzero p value to the uncertainty in $S_{\text{bulk}}[O(10^{-3})]$ pertaining to the variation in room temperature (24.8 °C–26.1 °C). No experiment was performed beyond $S_{\text{bulk}} = 1.029$, as it was difficult to keep the solution stable during handling. In Fig. 3(b), similar to the nucleation probability, we see an increase in the number of crystals formed (N) with both laser energy and bulk supersaturation above the minimum laser intensity threshold. We predominantly observed cubic crystals with the probability of finding a rectangle or needlelike crystal increasing with E and S_{bulk} (see Supplemental Material [23], Sec. V). This observed change in morphology aligns with previous observations [57,58], deduced using limited solvent availability per nuclei. In our experiments, we cannot measure local fluid properties surrounding the bubble, such as temperature and solute concentration, due to the small length and time scales involved. Therefore, we employ numerical simulations to calculate temporal and spatial values of these variables, while the experimentally measured bubble radii and crystal count are used to validate the fluid flow and local supersaturation, respectively.

In numerical simulations, we solve for combined momentum, heat, and solute transport. For each phenomenon, the governing equations for an unbound 3D sphere are used due to the plane of symmetry offered by the cover glass. We employ the Rayleigh-Plesset equation [59] to solve for the momentum surrounding the bubble,

$$R\frac{d^2R}{dt^2}+\frac{3}{2}\left(\frac{dR}{dt}\right)^2=\frac{1}{\rho_{\text{L}}}\left(p_{\text{V}}-p_\infty-\frac{2\sigma}{R}-\frac{4\mu}{R}\frac{dR}{dt}\right), \quad (1)$$

where $\rho_{\text{L}} = 1175\ \text{kg/m}^3$ is the solution density, $p_\infty = 1.013$ bar is the ambient pressure and p_{V} is the pressure within the bubble, σ is the surface tension, μ is the dynamic viscosity of the solution, and R is the distance of the interface from the laser focal point. The spherically symmetric heat dissipation surrounding the bubble is modeled using

$$\frac{\partial T}{\partial t}+\frac{R^2}{r^2}\frac{dR}{dt}\frac{\partial T}{\partial r}=\frac{1}{r^2}\frac{\partial}{\partial r}\left(r^2\alpha\frac{\partial T}{\partial r}\right), \quad (2)$$

in which T is the temperature, α is the thermal diffusivity of the solution, and r ($> R$) is the radial position from the bubble center. For solute transport, we use an analogous equation to Eq. (2) by substituting T with C^*, the solute concentration in kg/kg of the solution, and α with D, the mass diffusivity of the solute.

For simplicity, we assume the bubble to be a lumped system with an energy balance given by

$$\frac{d(m_{\text{V}}c_{p\text{V}}T_{\text{V}})}{dt}+\frac{dm_{\text{V}}}{dt}H_{\text{L}}=A_{\text{V}}k\left(\frac{\partial T}{\partial r}\right)_{r=R}, \quad (3)$$

where m_{V}, A_{V}, and $c_{p\text{V}}$ are the mass, surface area, and specific heat capacity of the vapor bubble, respectively. H_{L} is the latent heat of vaporization and k is the thermal conductivity of the solution. At the interface, we enforce the boundary condition $T_{\text{V}} = T|_{r=R}$ at all times, where T_{V} is the bubble temperature. The change in mass of the bubble is estimated using the corrected Hertz-Knudsen equation [60], $dm_{\text{V}}/dt = -(16A_{\text{V}}/9\sqrt{2\pi \text{R}_{\text{G}}T})[p_{\text{V}} - p_{\text{sat}}(T|_{r=R})]$, where R_{G} is the specific gas constant for water vapor and $p_{\text{sat}}(T|_{r=R})$ is the saturation pressure of the solution at the interface. The p_{V} is estimated using the ideal gas law, $p_{\text{V}}V_{\text{V}} = m_{\text{V}}\text{R}_{\text{G}}T_{\text{V}}$, where V_{V} is the bubble volume.

At $t = 0$ the bubble is assumed to be saturated with zero interface velocity, and the surrounding solute concentration is assumed to be same as in the bulk. System energy is imposed by initializing a thermal boundary layer profile surrounding the bubble. The initial temperature distribution is $T(\xi) = T_\infty + (T_{\text{V}} - T_\infty)\exp[-(\xi/\delta_{\text{T}})^{25}]$, where T_∞ is the ambient temperature, δ_{T} is the thermal boundary layer thickness, and $\xi = r - R$, is the radial distance from the interface. A high exponent of 25 is used to approximate a step function, while still being smooth enough to avoid numerical instabilities near $\xi \approx \delta_{\text{T}}$. The thermal energy supplied in the simulation is transformed into latent heat (vapor), sensible heat (vapor and liquid), and kinetic energy of the solution. Thus, the control parameter in simulation δ_{T} characterizes the energy available for a bubble to grow. The initial bubble temperature is chosen to be 650 K—the spinodal temperature [61], with the radius 0.5 μm calculated using theoretical laser spot dimensions. For details on the numerical model and parameter values solved, refer to the Supplemental Material [23], Sec. VI.

Figure 2(b) shows the numerically obtained bubble size for $\delta_{\text{T}} = 21$, 25.5, 29.5, 32.5, 34.5, and 36 μm, corresponding to the increasing laser energy values from experiments (see Supplemental Material [23], Sec. VI for calculations). The deviation between experiments and simulations in R for higher energies ($E \geq 90$ μJ) can be attributed to nonlinear absorption [62,63] with possible plasma formation. The plasma can initiate high pressures,

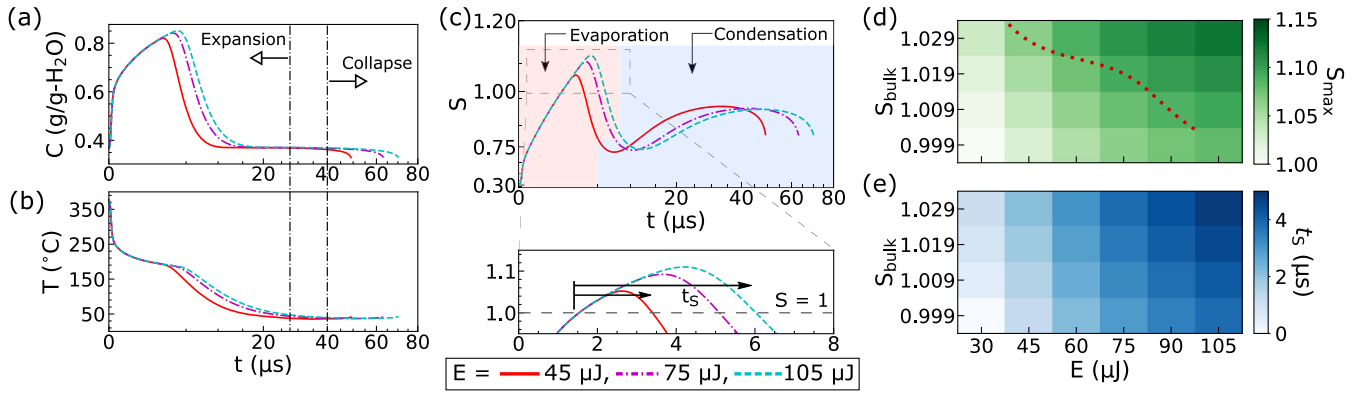

FIG. 4. (a),(b) Simulated temporal change in solute concentration (C) and temperature (T) at the interface for $S_{\mathrm{bulk}} = 1.019$ (at 25 °C). Since the laser pulse duration (4 ns) is negligible compared to the timescale of the phenomena (microsecond), we consider the energy transfer from the laser (E) to the solution to be instantaneous at $t = 0$ (x axis is scaled quadratically). (c) The supersaturation ratio calculated using the concentration and temperature plotted in (a) and (b), respectively. The x-axis scale is quadratic, while the y-axis scale is cubic. t_S represents the time period for which $S > 1$. (d) The simulated maximum S values obtained for all the conditions in this Letter, similar to the examples from (c). The red dotted curve is the guide to the eye from Fig. 3, representing the crystallization probability ≥ 0.5 in experiments. (e) The time period for which the simulated $S > 1$, similar to the examples from (c).

leading to higher interface velocities [64]. The probability of bubble incidence with and without $KMnO_4$ in water was investigated for nonlinear absorption, which supports the reasoning made for deviations in R (see Supplemental Material [23], Sec. I). Moreover, the increase in interface velocities will only enhance the solvent accumulation at the interface supporting our hypothesis (see Supplemental Material [23], Sec. VI).

To get insight into the crystal formation surrounding the bubble, we look at the factors affecting the solute supersaturation using simulation. Figures 4(a) and 4(b) show the temporal evolution of the solute concentration and temperature at the dynamic interface for three different laser energies at fixed bulk supersaturation. Initially, the temperature drops abruptly, in conjunction with a steep rise in concentration due to high evaporation rates, $O[100\ \mathrm{kg/(m^2\,s)}]$. Then, the decrease in temperature is more gradual, while the decrease in concentration is steep. The drop in temperature can be attributed to heat diffusion away from the interface and advection resulting from bubble dynamics. Similarly, for the solute, there is dilution occurring at the interface due to condensation of the vapor in addition to diffusion and advection. During the latter half of the bubble lifetime, the concentration and temperature have minimal change due to lower driving potentials and short time range, $O(10\ \mu\mathrm{s})$. The temperatures during bubble collapse estimated from the simulations are in good agreement with the empirical calculations from literature (see Supplemental Material [23], Sec. IV).

Figure 4(c) shows the temporal supersaturation at the interface calculated using profiles given in Figs. 4(a) and 4(b). We observe a peak in the local supersaturation ratio when the bubble is rapidly expanding, after which the supersaturation decreases and the interface stays undersaturated ($S < 1$) within the bubble lifetime. This observation of a momentarily supersaturated state ($S > 1$), highlighted in the close-up in Fig. 4(c), is a favorable condition for crystal nucleation. Moreover, both the peak supersaturation (S_{max}) and the time during which the interface remains supersaturated (t_S) increase with increasing E. In the above analysis, we only look at the interface since heat diffuses faster than the solute and thus the maximum supersaturation ratio can exist only in the region closest to the bubble, i.e., at the interface. The estimated supersaturated layer thickness increases with E and is $O(10\ \mathrm{nm})$, consistent with literature [21]. However, this supersaturation ratio at the interface is dynamic and is quantified only when the bubble exists. The induced flow and resulting temperature and solute distribution surrounding the laser focal point after the bubble collapses are complex and outside the scope of this work. The simulated trends observed in Figs. 4(d) and 4(e) agree well with the presented experimental results in Fig. 3.

Subsequently, we correlate the simulated crystallization parameters S_{max} and t_S with the experimentally acquired parameter N [Fig. 3(b)]. The nucleation rate (the number of nuclei formed per unit time per unit volume) can be expressed as [65]

$$J \propto S \exp\{-16\pi v^2\gamma^3/[3k_B^3T^3\log^2(S)]\}, \tag{4}$$

where γ is the solute-solution interfacial tension, k_B is Boltzmann's constant, and v is the molecular volume. We relate $J \propto N/t_S$. Since the size of the bubbles for the time region where $S > 1$ are almost the same within the range of energies used, we leave out the shell volume surrounding the interface in the proportionality for J. Using the slope from Fig. 5(a), we estimate γ in Eq. (4) to be $3.7^{+0.47}_{-0.65}\ \mathrm{mJ/m^2}$ (at ≈185 °C–191 °C). This value, when calculated for 25 °C (3.51 $\mathrm{mJ/m^2}$), is within the reported

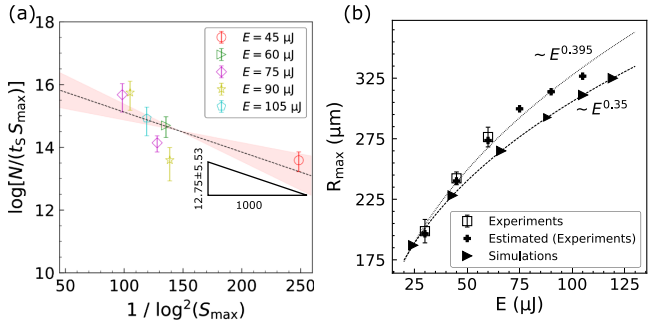

FIG. 5. (a) Estimate of nucleation rate J against simulated peak supersaturation ($S_{\max}$). $J \propto N/t_S$, where N is the mean crystal count from experiments and t_S is the time for which $S > 1$ in simulations. (b) Maximum vapor bubble radius plotted against the energy supplied. The dotted and dashed lines represent the power law fit for the data from experiments and simulations, respectively. Error bars represent the standard error on the mean.

values of 2.19–5.283 $\mathrm{mJ/m^2}$ for NPLIN [66–68] (see Supplemental Material [23], Sec. VII for calculation). Note that the elevated temperature is also a favorable condition for crystal nucleation in addition to supersaturation [Eq. (4)].

Figure 5(b) is an equivalent representation of Fig. 2(b), showing the dependence of maximum bubble size ($R_{\max}$) for varying supplied energies. The estimate of the $R_{\max}$ in experiments was made using the bubble lifetime [69,70] (see Supplemental Material [23], Sec. VIII). The closely matching trends between experiments and simulations support the reliability of the boundary conditions and assumptions employed in the simulation.

In summary, we have shown that primary nucleation in supersaturated aqueous KCl solution can be triggered by thermocavitation induced by a single Nd:YAG laser pulse below the optical breakdown threshold. The nucleation probability as well as the number and morphology of crystals formed depends on bulk supersaturation and laser energy used. Combining high-speed microscopy experiments and finite element simulations, we propose a nucleation mechanism based on the solute accumulation at the interface due to solvent evaporation into the growing bubble. Simulations reveal a momentary spike in supersaturation with a lifetime [$O(\mu s)$] proportional to the bulk supersaturation and the supplied laser energy to facilitate nucleation.

The proposed mechanism is distinct from other speculated routes to crystal nucleation in laser-induced cavitation experiments, for example, due to photochemistry [71] and shock waves [72]. The intentional addition of $KMnO_4$ enabled bubble formation via thermocavitation avoiding photochemistry—which otherwise might exist due to plasma in cavitation via optical breakdown. Furthermore, our calculations reveal the length scale of shockwave influencing crystallization [$O(10\ \mu m)$] matches the thermal boundary layer thickness surrounding the bubble (see Supplemental Material [23], Sec. VIII). Therefore, we expect no formation of crystals due to shock waves because of the lower supersaturation ratio associated with higher temperatures. Thus, the proposed mechanism, verified by combining experiments and simulations, may shed light on the discussion of the working mechanism(s) behind NPLIN and sonocrystallization via cavitation [73,74].

This work was funded by LightX project under Nederlandse Organisatie voor Wetenschappelijk Onderzoek Open Technology Programme (Project No. 16714). We thank Dr. D. Irimia and Ing. E. F. J. Overmars for supporting the experiments, and Sára Bánovská for supporting the solubility tests. A special thanks to Dr. H. J. M. Kramer, Dr. A. E. D. M. van der Heijden, and members of the LightX user committee for the productive discussions.

*h.b.eral@tudelft.nl

[1] D. Kashchiev, *Nucleation: Basic Theory with Application* (Butterworth-Heinemann, London, 2000), Vol. 1.
[2] J. W. Mullin, *Crystallization* (Butterworth-Heinemann, Oxford, 2001).
[3] A. S. Myerson and B. L. Trout, Science **341**, 855 (2013).
[4] C. Schoonen and J. F. Lutsko, Phys. Rev. Lett. **129**, 246101 (2022).
[5] J. F. Lutsko, Sci. Adv. **5**, eaav7399 (2019).
[6] V. Bianco, P. M. de Hijes, C. P. Lamas, E. Sanz, and C. Vega, Phys. Rev. Lett. **126**, 015704 (2021).
[7] R. Grossier, Z. Hammadi, R. Morin, and S. Veesler, Phys. Rev. Lett. **107**, 025504 (2011).
[8] G. Díaz Leines and J. Rogal, Phys. Rev. Lett. **128**, 166001 (2022).
[9] M. B. Bigdeli and P. A. Tsai, Langmuir **36**, 4835 (2020).
[10] B. A. Garetz, J. E. Aber, N. L. Goddard, R. G. Young, and A. S. Myerson, Phys. Rev. Lett. **77**, 3475 (1996).
[11] M. N. Hussain, J. Jordens, S. Kuhn, L. Braeken, and T. Van Gerven, Chem. Eng. J. **408**, 127272 (2021).
[12] C. Duffus, P. J. Camp, and A. J. Alexander, J. Am. Chem. Soc. **131**, 11676 (2009).
[13] B. A. Garetz, J. Matic, and A. S. Myerson, Phys. Rev. Lett. **89**, 175501 (2002).
[14] Y. Liu, M. H. van den Berg, and A. J. Alexander, Phys. Chem. Chem. Phys. **19**, 19386 (2017).
[15] A. J. Alexander and P. J. Camp, Cryst. Growth Des. **9**, 958 (2009).
[16] A. J. Alexander and P. J. Camp, J. Chem. Phys. **150**, 040901 (2019).
[17] E. Zwaan, S. Le Gac, K. Tsuji, and C.-D. Ohl, Phys. Rev. Lett. **98**, 254501 (2007).
[18] Y. Arita, M. Antkowiak, V. Venugopalan, F. J. Gunn-Moore, and K. Dholakia, Phys. Rev. E **85**, 016319 (2012).
[19] L. Wang, Y. Wu, X. Wu, and K. Cen, Exp. Therm. Fluid. Sci. **121**, 110266 (2021).
[20] V. Korede, N. Nagalingam, F. M. Penha, N. van der Linden, J. T. Padding, R. Hartkamp, and H. B. Eral, Cryst. Growth Des. **23**, 3873 (2023).
[21] N. Hidman, G. Sardina, D. Maggiolo, H. Ström, and S. Sasic, Cryst. Growth Des. **20**, 7276 (2020).

[22] J. J. Schoppink, J. Krizek, C. Moser, and D. Fernandez Rivas, Exp. Therm. Fluid. Sci. **146**, 110926 (2023).
[23] See Supplemental Material at http://link.aps.org/supplemental/10.1103/PhysRevLett.131.124001 for experimental methodology, details on numerical model, and other miscellaneous calculations, which includes Refs. [24–50].
[24] P. A. Quinto-Su, M. Suzuki, and C.-D. Ohl, Sci. Rep. **4**, 5445 (2014).
[25] C. Matzler, MATLAB functions for Mie scattering and absorption, Institut für Angewandte Physik (2002).
[26] M. R. Querry, Optical constants, Technical Report CRDC-CR-85034 (Missouri University, Kansas City, 1985).
[27] J. R. Wood, Geochim. Cosmochim. Acta **40**, 1211 (1976).
[28] L. Rayleigh, London, Edinburgh, and Dublin Philos. Mag. J. Sci. **34**, 94 (1917).
[29] R. G. Lunnon, Proc. Phys. Soc. London **25**, 180 (1912).
[30] H. Ozbek and S. L. Phillips, Thermal conductivity of aqueous NaCl solutions from 20 °C to 330 °C, Technical Report, U.S. Department of Energy, 1979, 10.2172/6269880.
[31] J. D. Toner and D. C. Catling, J. Chem. Eng. Data **62**, 995 (2017).
[32] J. Kestin, H. E. Khalifa, and R. J. Correia, J. Phys. Chem. Ref. Data **10**, 57 (1981).
[33] O. Ozdemir, S. I. Karakashev, A. V. Nguyen, and J. D. Miller, Miner. Eng. **22**, 263 (2009).
[34] E. S. Nowak and R. J. Grosh, An analysis of specific heat data for water and water vapor in the critical region, Technical Report No. 8, U.S. Department of Energy, 1961, 10.2172/4832052.
[35] H. G. Leopold and J. Johnston, J. Am. Chem. Soc. **49**, 1974 (1927).
[36] Y. C. Chang and A. S. Myerson, AIChE J. **31**, 890 (1985).
[37] Reference Manual, COMSOL Multiphysics v. 5.6, 2020, https://www.comsol.com/release/5.6.
[38] J. Kestin, M. Sokolov, and W. A. Wakeham, J. Phys. Chem. Ref. Data **7**, 941 (1978).
[39] G. W. Preckshot and G. G. Brown, Ind. Eng. Chem. **44**, 1314 (1952).
[40] A. C. Chatterji and R. N. Singh, J. Phys. Chem. **62**, 1408 (1958).
[41] A. Faravar and M. Manteghian, Int. J. New Chem. **6**, 43 (2019).
[42] A. Mersmann, J. Cryst. Growth **102**, 841 (1990).
[43] V. L. Thurmond, R. W. Potter II, and M. A. Clynne, The densities of saturated solutions of NaCl and KCL from 10 degrees to 105 degrees C, Technical Report, U.S. Geological Survey, 1984, 10.3133/ofr84253.
[44] V. Venugopalan, A. Guerra, K. Nahen, and A. Vogel, Phys. Rev. Lett. **88**, 078103 (2002).
[45] R. Hickling, Phys. Rev. Lett. **73**, 2853 (1994).
[46] M. H. Rice and J. M. Walsh, J. Chem. Phys. **26**, 824 (1957).
[47] N. Mirsaleh-Kohan, A. Fischer, B. Graves, M. Bolorizadeh, D. Kondepudi, and R. N. Compton, Cryst. Growth Des. **17**, 576 (2017).
[48] Y. Darojat, A. Aljalal, K. Gasmi, I. H. Aljundi, N. Mirsaleh-Kohan, and W. Al-Basheer, ACS Omega **7**, 38400 (2022).
[49] G. K. Batchelor, *An Introduction to Fluid Dynamics* (Cambridge University Press, Cambridge, England, 1967).
[50] O. Supponen, Collapse phenomena of deformed cavitation bubbles, Technical Report 8089, EPFL, 2017.
[51] R. Kacker, S. Dhingra, D. Irimia, M. K. Ghatkesar, A. Stankiewicz, H. J. M. Kramer, and H. B. Eral, Cryst. Growth Des. **18**, 312 (2018).
[52] T. Sugiyama and S.-F. Wang, J. Photochem. Photobiol., C **52**, 100530 (2022).
[53] F. Reuter, C. Deiter, and C.-D. Ohl, Ultrason. Sonochem. **90**, 106131 (2022).
[54] O. Supponen, D. Obreschkow, M. Tinguely, P. Kobel, N. Dorsaz, and M. Farhat, J. Fluid Mech. **802**, 263 (2016).
[55] N. Nagalingam, A. Raghunathan, V. Korede, E. F. Overmars, S.-T. Hung, R. Hartkamp, J. T. Padding, C. S. Smith, and H. B. Eral, HardwareX **14**, e00415 (2023).
[56] P. A. Quinto-Su, K. Y. Lim, and C.-D. Ohl, Phys. Rev. E **80**, 047301 (2009).
[57] J. Kardum, A. Sander, and A. Glasnoviae, Chem. Biochem. Eng. Q. **19**, 39 (2005).
[58] A.-C. Cheng, H. Masuhara, and T. Sugiyama, J. Phys. Chem. C **124**, 6913 (2020).
[59] M. S. Plesset and A. Prosperetti, Annu. Rev. Fluid Mech. **9**, 145 (1977).
[60] J. Barrett and C. Clement, J. Colloid Interface Sci. **150**, 352 (1992).
[61] R. Thiéry and L. Mercury, J. Solution Chem. **38**, 893 (2009).
[62] J. Noack and A. Vogel, IEEE J. Quantum Electron. **35**, 1156 (1999).
[63] W. Sun, Z. Liu, and H. Zhou, J. Nanosci. Nanotechnol. **16**, 3895 (2016).
[64] A. Vogel, S. Busch, and U. Parlitz, J. Acoust. Soc. Am. **100**, 148 (1996).
[65] D. Kashchiev and G. M. van Rosmalen, Cryst. Res. Technol. **38**, 555 (2003).
[66] K. Fang, S. Arnold, and B. A. Garetz, Cryst. Growth Des. **14**, 2685 (2014).
[67] A. J. Alexander and P. J. Camp, Cryst. Growth Des. **9**, 958 (2009).
[68] M. R. Ward and A. J. Alexander, Cryst. Growth Des. **12**, 4554 (2012).
[69] B. Han, K. Köhler, K. Jungnickel, R. Mettin, W. Lauterborn, and A. Vogel, J. Fluid Mech. **771**, 706 (2015).
[70] K. R. Rau, P. A. Quinto-Su, A. N. Hellman, and V. Venugopalan, Biophys. J. **91**, 317 (2006).
[71] T. Okutsu, K. Furuta, M. Terao, H. Hiratsuka, A. Yamano, N. Ferté, and S. Veesler, Cryst. Growth Des. **5**, 1393 (2005).
[72] B. Lindinger, R. Mettin, R. Chow, and W. Lauterborn, Phys. Rev. Lett. **99**, 045701 (2007).
[73] J. Lee, K. Yasui, M. Ashokkumar, and S. E. Kentish, Cryst. Growth Des. **18**, 5108 (2018).
[74] A. Bussonnière, Q. Liu, and P. A. Tsai, Phys. Rev. Lett. **124**, 034501 (2020).